Small Atom Doping: A Synergistic Strategy to Reduce Sn_{Zn} Recombination Center Concentration in $Cu_2ZnSnSe_4$

Alex Jimenez-Arguijo,* Alejandro Navarro Güell, Yudania Sanchez, Claudia Malerba, Matteo Valentini, Pascal Becker, Leo Choubrac, Thomas Unold, Zacharie Jehl Li-Kao, Sergio Giraldo, and Edgardo Saucedo*

Kesterite $Cu_2ZnSnS_xSe_{4-x}$ (CZTSSe) is among the most promising inorganic Earth-abundant thin-film photovoltaic technologies, although currently, the larger voltage deficit compared with more mature chalcogenide technologies is hampering solar-to-electricity conversion efficiency progress in these materials. Most of the latest reports agree on the CZTSSe defect structure as the main limitation for the open-circuit voltage. Small atom doping is suggested as an interesting strategy to reduce the concentration of defects without affecting secondary phase formation. Herein, an innovative approach based on the introduction of $LiAlH_4$ and its further decomposition during the selenization process of CZTSe precursors, as a pathway for hydrogen and lithium/alkali transient doping, is explored. This process shows a strong beneficial influence on the crystal growth and solar cell device performance, especially with a significant improvement in V_{oc} and fill factor. A reduction of nonradiative recombination and a remarkable fourfold increase in the carrier lifetime correlating with the reduction of the open-circuit voltage (V_{oc}) deficit below 330 mV is demonstrated. A mechanism on how small atoms (Li and H) interact to reduce the concentration of Sn_{Zn} recombination centers while keeping doping relatively unchanged is proposed, opening fundamental perspectives for the simple and universal transient doping of thin-film chalcogenide compounds.

1. Introduction

Thin-film photovoltaic (PV) technologies have emerged from the need of achieving truly low-cost modules for energy production that are economically competitive with nonrenewable combustion-based energy sources. Mass production of thin-film modules would allow for building- and product-integrated photovoltaics (BIPV and PIPV), identified as the key enabling technologies to make "near-zero-energy buildings" and "net-zero-energy districts" more realistic. Currently, thin-film PV technologies which have reached competitive power conversion efficiencies (PCE) beyond 20% are based on $Cu(In,Ga)S_xSe_{2-x}$ (CIGSSe) and CdTe absorber materials.[1–3] Unfortunately, the aforementioned mature technologies make use of scarce and expensive (In, Ga, Te) or toxic elements (Cd).

Therefore, developing PV technologies based on Earth-abundant and fully sustainable materials is required. Kesterite $Cu_2ZnSnS_xSe_{4-x}$ (CZTSSe) is currently one of the most promising emerging fully inorganic thin-film PV technologies based exclusively on Earth-abundant elements thanks to its tunable bandgap (from 1.0 to 1.5 eV) and high absorption coefficient ($>10^4 \, cm^{-1}$).[4–6] Nevertheless, the efficiency of CZTSSe-based solar cells has plateaued around 12-13% for as much as 7 years, hindering CZTSSe-based devices from becoming environmentally cost-effective.[1,7–11] It is well known that the main limiting factor in CZTSSe devices is the large open-circuit voltage (V_{oc}) deficit.[12,13] Short-circuit current (J_{sc}) is not considered a critical parameter since it can be greatly enhanced optimizing the optical configuration of the device, resulting in many CZTSSe efficient devices achieving more than 80% of the Shockley–Queisser limit J_{sc} (J_{sc}^{SQ}).[7–9,11,12] Also, fill

A. Jimenez-Arguijo, Y. Sanchez
Solar Energy Materials and Solar Cells (SEMS)
Catalonia Institute for Energy Research (IREC)
08930 Barcelona, Spain
E-mail: ajimenez@irec.cat

The ORCID identification number(s) for the author(s) of this article can be found under https://doi.org/10.1002/solr.202200580.

A. Jimenez-Arguijo, A. Navarro Güell, Z. Jehl Li-Kao, S. Giraldo, E. Saucedo
Photovoltaic Group
Electronic Engineering Department
Polytechnic University of Catalonia (UPC)
08034 Barcelona, Spain
E-mail: edgardo.saucedo@upc.edu

C. Malerba, M. Valentini
Italian National Agency for New Technologies
Energy and Sustainable Economic Development (ENEA)
00123 Roma, Italy

P. Becker, L. Choubrac, T. Unold
Department Structure and Dynamics of Energy Materials
Helmholtz-Zentrum Berlin für Materialien und Energie GmbH
14109 Berlin, Germany

factor (FF) values for CZTSSe technologies are still below commercially required values.[7] The main limitation of FF is the high recombination rates, which also limit the V_{oc}. The FF in CZTSSe is also affected by an intrinsically high series resistance associated with thick and resistive MoS_xSe_{2-x} layers and secondary phase segregation at the back contact (e.g., ZnS_xSe_{1-x}), the latter being more relevant for S-rich CZTSSe.[14]

Several origins for the V_{oc} deficit have been proposed, which can be mainly ascribed to three regions of the device: 1) the CZTSSe/CdS interface, 2) the CZTSSe/Mo interface (i.e., the back contact), and 3) the bulk of CZTSSe. While still relevant for CZTSe absorbers, losses at front and back contacts become more relevant for S-rich CZTSSe absorbers. It has been identified that for the Se-rich composition the main recombination pathways lie in the space-charge region (SCR), that is, in the bulk of the absorber.[14–22]

Since the potential of kesterite materials as photovoltaic absorbers was identified, most of the publications have aimed to suppress the numerous detrimental effects of the proliferating secondary phases, while optimizing carrier concentration by controlling the Cu, Zn, Sn, and S/Se chemical potentials, that is, optimizing intrinsic doping.[23–26] This leads to constraints on the growth conditions to a compositional region where the impact of secondary phases is minimum. However, the effects of this optimization on the recombination center concentration were majorly disregarded, resulting in minority carrier lifetimes of less than 1 ns.[27] Comparing CZTSSe minority carrier lifetime with its Earth-scarce element parent technology ($CuInGaSe_2$, CIGSe) which shows lifetimes of more than 50 ns can explain why the CIGSe technology is already at 23% efficiency while CZTSSe is at 13%.[2]

Efforts toward identifying the main cause of high nonradiative, that is, Shockley–Read–Hall (SRH), recombination rates, leading to low minority carrier lifetimes, have been made in the latter years. The first suggested deterrent was the Cu–Zn disorder, leading to bandgap and electrostatic potential fluctuations enhancing recombination rates.[28–32] Another strongly suggested bulk origin of the high nonradiative recombination rates is the nonpassivated grain boundaries and/or the presence of bulk intrinsic recombination centers.[33–38]

Recent advances in the microscopic description of recombination processes have been developed, allowing Kim et al.[13] to calculate the SRH recombination rates for each point defect present in the CZTSe bulk using the defect concentrations and carrier capture cross sections obtained by DFT calculations.[13,39–42] Then, it was identified that the origin of low-minority carrier lifetime is essentially related to the presence of Sn-related deep defects, specifically Sn_{Zn}. The presence of this defect would result in subnanosecond lifetime values in accordance with the estimated experimental values of hundreds of picoseconds.[13,27,43]

Hence, the bulk of Se-rich CZTSSe is currently limiting the V_{OC}, especially the short minority carrier lifetime due to the presence of Sn_{Zn} recombination centers. Currently, the main technological challenge lies in the fact that lifetime should be increased without strongly modifying the secondary phase formation and the majority carrier concentration, that is, without modifying intrinsic doping. In this work we want to point out the fact that Sn_{Zn} defects present a donor behavior (i.e., the formation energy increases with E_F). Thus, the following interplay arises: if the

Fermi Energy (E_F) is too high, the V_{oc} will be limited by the low hole concentration. Alternatively, if it is too low, it will be limited by the high recombination center concentration. In consequence, the dependence of both secondary phase formation and defect structure on intrinsic doping (i.e., Cu, Zn, and Sn chemical potentials) indicates a limitation on the bulk performance of CZTSSe in equilibrium conditions. Note that E_F position in the bandgap determines both carrier concentration and deep defect concentration, with opposite trends. Hence, in order to overcome the 13% efficiency bar, it is necessary to explore out-of-equilibrium conditions by means of transient extrinsic doping.

Exploiting the apparently disadvantageous fact that Sn_{Zn} is a donor, a transient upward E_F shift (i.e., only during growth) has been suggested as a potential promising strategy to reduce the concentration of Sn antisite defects, while returning to (or even improving) the desired p-type conductivity after the cooling down of the sample.[13] This treatment therefore would allow for the decoupling of carrier concentration, determined by Cu–Zn defects (V_{Cu}, Zn_{Cu}, and Cu_{Zn}), and lifetime, mainly controlled by Sn deep defects (Sn_{Zn}). Yuan et al. suggested a similar transient mechanism in order to explain the enhanced p-type conductivity of NaF-doped CIGS, which was not possible to explain with traditional doping theory.[44] Indeed, a permanent upward E_F shift (also increasing E_F during growth, when impurities present increased solubility) doping by means of Ga_{Zn} defect formation has been shown to increase V_{oc} even though hole concentration is reduced.[45] On the other hand, isovalent In doping has shown to be detrimental for V_{oc} while increasing hole concentration, related to the predominant formation of In_{Sn} instead of In_{Zn} due to the larger atomic size, and other III-valent atoms like B and Al would also act as donors.[46,47]

Achieving a transient upward E_F shift is a technologically challenging task, as it requires donor impurities at high temperature, which are able to outgas or become electrically inert at room temperature. Hydrogen is probably the most suitable atom for performing transient upward E_F shift due to the predicted low formation energy of H_i donor defects in CZTSe and CISe, as has been experimentally shown for CISe.[48,49] Other small atoms such as Li might have similar effects, although to a lesser extent. In addition, it has been shown that Na is able to migrate in CZTSSe via Cu vacancies at room temperature.[50,51] Thus, unless strong electrostatic interactions arise (i.e., bonding), atoms smaller than Na could show a similar behavior, allowing them to outgas or accumulate at the grain boundaries during the cooling down step, while their solubility decreases with temperature.

In this sense, controlled hydrogen doping during CZTSSe reactive annealing is not straightforward due to the high stability of H_2 and the high toxicity of $H_2(S,Se)$ or hydrazine in the case of solution-based CZTSSe. Interestingly, the former CZTSSe efficiency record of 12.62% was achieved under the effects of H_2S toxic gas.[8] In addition, in the past, high-efficiency solution-processed CZTSSe devices were grown from a pure hydrazine solution.[9,52] In these cases, the presence of H_i during growth cannot be completely discarded either, further supporting the hypothesis of increased E_F during growth, resulting in a better performance of CZTSSe absorber. The incorporation of H in the CZTS surface coming from Al_2O_3 atomic layer deposition has

been shown to improve CZTS device performance, either by grain boundary passivation or by selective surface doping.[53]

To achieve a transient upward E_F shift from the gas phase without the use of highly stable compounds and explosive or toxic hydrogen gases, the use of hydrides is explored. In this work, we focus on the effects of $LiAlH_4$ decomposition during the reactive annealing of Se-pure kesterite, where bulk nonradiative SRH recombination limits the minority carrier lifetime and thus, the V_{oc}. It is known that $LiAlH_4$ decomposes into its elemental components above its melting temperature of 125 °C.[54] Therefore, the presence of elemental Li, Al, and H during reactive annealing is expected above this temperature. Interestingly, the use of small alkali metals has already been reported as beneficial for CZTSSe with effects other than the aforementioned transient E_F upward shift, mainly affecting grain growth and grain boundary conditions, with strong evidence of grain boundary passivation effects.[11,33–35,55–57] In particular, Li has been reported to be the most promising alkali.[56,58] In fact, recently, the addition of lithium bis(tri-fluoromethanesulfonyl) imide (LiTFSI), to the solution-processed CZTSSe precursor held the record efficiency (12.7%) for kesterite-based devices.[11]

This work proposes a simple yet effective approach to reduce the recombination center concentrations of CZTSe absorbers while keeping the hole concentration high, thus reducing the V_{oc} deficit of the solar cell devices, by implementing the use of $LiAlH_4$ during the growth of the absorber CZTSe. Furthermore, the potential beneficial effect of this hydride is twofold, as at high temperatures it allows simultaneously for 1) Li treatment and 2) hydrogen treatment (upward E_F shift) from a gas phase, without the need of any additional step. This study includes a deep investigation and characterization of the effects of Li and H small atom transient doping on the material and device properties in CZTSe-based solar cells, opening fundamental perspectives for simple transient doping in thin-film chalcogenide compounds.

2. Results

2.1. Material Characterization and Photovoltaic Performance

First, a comparison of the effects of $LiAlH_4$ decomposition on the composition (XRF), morphology (SEM), and optoelectronic properties of CZTSe (J-V curves) for the two different thermal annealing profiles, that is, one-step and two-step selenization processes, will be presented. The compositions determined from the XRF measurements shown in Table S1, Supporting Information, do not reveal any significant changes in the cation ratio upon $LiAlH_4$ addition regardless of the thermal profile. There is a consistent loss of Sn with respect to Zn. The $Cu/(Zn + Sn)$ ratio of the samples is around 0.71 after selenization and Zn/Sn ratio is around 1.10, which are typical values for as-grown Cu-poor Zn-rich CZTSe absorbers. However, the Se/cation ratio shown in Figure S1b, Supporting Information, is dependent on both hydride mass and the thermal process. While reference samples for both one step and two step reveal the same ratio, the Se content slightly increases with $LiAlH_4$ mass for one step while it decreases for two step. In addition, selenization is more homogeneous for one-step processes if more hydride mass is added, as evidenced by XRF mapping. The latest could be explained by the formation of the well-known alkali–Se phases that can act as fluxing agents catalyzing selenization and grain growth at the annealing temperatures used in this work.[11,55,57]

The enhanced grain size revealed by the SEM cross-section images shown in **Figure 1** for one-step samples is a clear indication that Li–Se and/or Na–Se phases are present during selenization. The larger grains could imply an improved $CZTSe/MoSe_2$ contact, avoiding the formation of double-layer CZTSe with lesser presence of voids and cracks at the back side region of the CZTSe layer (see J-V discussion). This demonstrates that the presence of alkali during reactive annealing allows one-step processes to achieve appropriate grain growth
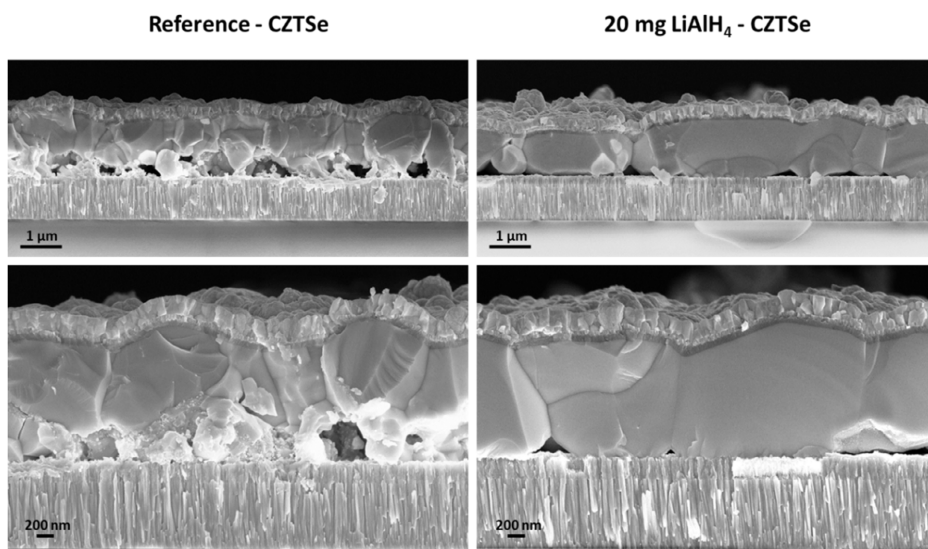

Figure 1. SEM cross-section images of the one-step process: reference and 20 mg $LiAlH_4$ samples are shown. An enhanced grain size is observed, as well as indication of grain coalescence, consequence of a liquid-assisted grain growth mechanism. The improvements in grain morphology and contact homogeneity are regarded as the first indicator of a process improving CZTSe quality.

and morphology with reduced processing time. Nevertheless, intriguingly for two-step processes, the grain size decreases with the hydride mass added during the selenization (Figure S2, Supporting Information). In this case, a reasonable explanation would be the longer and excessive exposure to alkali–Se phases from hydride decomposition because of the additional annealing step (additional 30 min). This detrimental effect of excessive alkali–Se phases on the CZTSe grain growth and optoelectronic performance has been previously reported, although a negative impact of excessive exposure to Al and/or H or the effects of the low-pressure step cannot be disregarded.[57]

Solar cell devices were completed for both sets of samples and in-depth characterizations were performed; the optoelectronic parameters are shown in Figure S3a, Supporting Information. The performance of the two-step set decreases with hydride mass while the one-step set reveals the opposite trend, showing remarkable performance improvement. This suggests, as it is well known, that good optoelectronic performance is restricted to Se-rich samples (avoiding the presence of V_{Se} deep defects), with good morphology/grain size, as long as good keserite phase purity is achieved without the presence of detrimental secondary phases or excessive MoSe$_2$ at the interface.[37] However, achieving Se-rich CZTSe and big grains with good morphology alone does not guarantee improved performances for kesterite solar cells.[59,60] Therefore, the one-step samples were thoroughly characterized to further elaborate on the impact of the LiAlH$_4$ treatment on the bulk recombination properties.

Figure S3b, Supporting Information, shows the illuminated J-V curves for one-step samples treated, indicating a clear improvement on all the optoelectronic parameters. The statistical distribution of the relevant optoelectronic parameters for the one-step annealed samples with different masses of LiAlH$_4$ as described in the Experimental Section is presented in **Figure 2**. The nominal relative ratios of the introduced Li and H over the total cation concentration, that is, $\frac{[Li]}{[Sn]+[Zn]+[Cu]}$ and $\frac{[H]}{[Sn]+[Zn]+[Cu]}$ for 20 mg of LiAlH$_4$, are 14 and 57 respectively, the maximum number (if every atom introduced acts as dopant) of supplied Li and H atoms to the system being 3.7×10^{20} Li and 1.27×10^{21} H atoms. If only 10% of the hydrogen atoms act as donor dopants, the effects of the transient upward E_F shift should be observed, according to the study by Kim et al.[13] **Figure 3**a) presents the corresponding EQEs, including the reflectance losses of the complete devices. Upon addition of 20 mg of LiAlH$_4$ the efficiency increases from 6.9% (reference CZTSe) to 8.9% (CZTSe-20 mg), achieving an impressive V_{oc} of 469 mV in the first optimization, resulting in a V_{oc} deficit ($V_{oc}^{Def} = V_{oc}^{SQ} - V_{oc}^{Measured}$, where $V_{OC}^{SQ} = 0.928$ $E_g/q - 0.176$ V) of ≈ 330 mV, one of the lowest V_{oc} deficits reported for kesterite devices, as shown in **Table 1**. J_{sc} slightly increases from 27.1 to 27.4 mA cm^{-2}. Unfortunately, this is in disagreement with the current calculated from the EQE measurements (from 26.8 to 30.2 mA cm^{-2}), which shows a more remarkable increase in short-circuit current. Current losses in the devices are related to nonoptimized window layer reflection and absorption, implying that further efficiency improvements could be achieved. Using optical simulations, we find that with an antireflective coating (ARC), a maximum current gain of
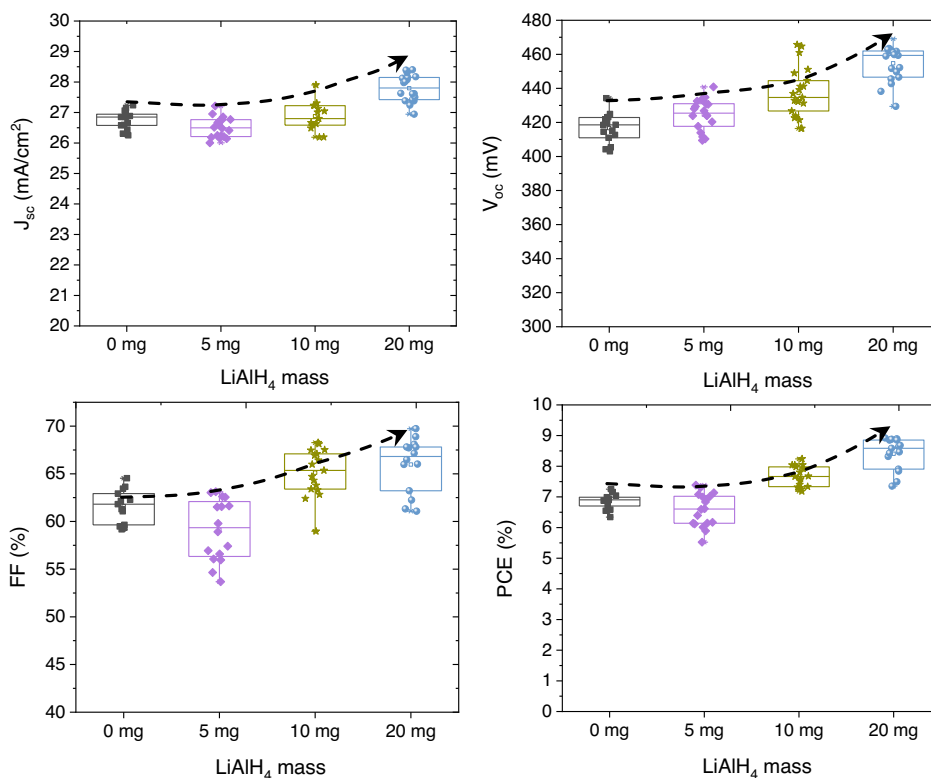

Figure 2. Statistics of the optoelectronic parameters for the 1-step selenization samples. Improvement in all optoelectronic parameters is observed.
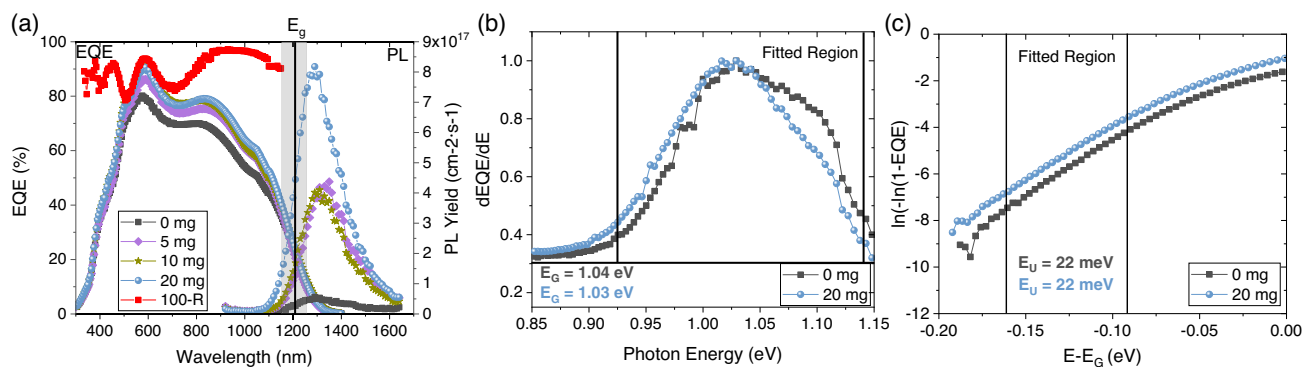
Figure 3. a) EQE curves of the one-step set of samples. Averaged PL emission spectra shown on the right. Best subcell measurement of each sample is shown. Reflectance losses are included. b) EQE derivative used to extract E_G position and standard deviation from EQE data. c) Urbach energy extracted from the sub-E_G region of the EQE spectra.

Table 1. V_{oc} deficits of the most efficient CZTSSe devices reported.

Reference	E_g [eV]	V_{oc} [mV]	V_{oc} deficit [meV]	Relevant features
This work	1.04	469	330	CZTSe–sputtering–transient doping
[9]	1.04	490	310	CZTSe–sputtering–Pre-selenization
[45]	1.14	515	380	CZTSSe–sputtering–Ga^{3+} incorporation
[8]	1.13	541	345	CZTSSe–sputtering–H$_2$S anneal
[10]	1.5	730	500	CZTS–sputtering–heterojunction heat treatment
[7]	1.13	513	370	CZTSSe–solution processed–hydrazine
[11]	1.05	477	330	CZTSSe–solution processed–LTFSI doping
[61]	1.06	507	310	CZTSSe–solution processed (Sn^{4+})
[62]	1.07	526	310	CZTSSe–solution processed (method of 61) (CZTSSe/Al$_2$O$_3$/AZTSSe)
[63]	1.07	540	290	ACZTSSe–solution processed (method of 61)
[64]	1.11	514	350	CZTSSe–solution processed–carbon framework

2.5 mA cm^{-2} could be achieved. Using the more accurate J_{sc} extracted from the EQE and considering the current gain that would be obtained using an ARC, we approximate the optically optimized current of the cell to be around 32 mA cm^{-2}. By taking into consideration the optically optimized current, the maximum achievable efficiency of the device is 10.3%. Using optimized window layer conditions has shown that there is a 5 mA cm^{-2} loss due to window layer properties; therefore, we postulate the possibility of further increasing the current to 34-35 mA cm^{-2} and a projected efficiency of 11.3%.

The EQE spectra ratios shown in Figure S4, Supporting Information, suggest both an increased junction quality/reduced depletion region recombination related to an increase in the short-wavelength region collection efficiencies and an improved collection length in the quasineutral region (QNR) related to a monotonic increase in the long-wavelength region with the LiAlH$_4$ mass. All LiAlH$_4$-treated samples exhibit an improvement in device performance in the long-wavelength region, while

at least 10 mg are needed to maximize the improvement in the short-wavelength region. In the literature, Li surface selective alloying has been predicted and shown to increase the junction quality by improved band alignment, morphology, and reducing shunt paths and therefore improving J_{sc} and FF.[55,65] Further studies on the modifications of the process on the CZTSe/CdS interface and the CZTSe surface quality should be performed in order to shed light on the short-wavelength region improvement of CZTSe solar cells. Either the incorporation of H_i or a reduction of Cu_{Zn} antisites at the surface could result in an improved band alignment with the CdS by an improved-type inversion before the junction.

In-depth compositional profiles for Cu, Zn, Sn, Se, Mo, Na, Li, Al, and H were determined by glow discharge optical emission spectroscopy (GDOES) (see **Figure 4**a). Al is not detected in either of the samples, probably due to the high formation energy of Al^{3+} defects, related to the fact that no 3$^+$ cations are present in the CZTSe matrix, added to the high formation temperature of Al$_2$Se$_3$, limiting the role of Al during the CZTSe growth.[66] Hydrogen detection was not achieved either as GDOES is not a reliable technique for measuring hydrogen traces since the detection threshold is relatively high. Although hydrogen is expected to outgas from the material (similarly to Li and to a lesser extent Al), the presence of trace concentrations of hydrogen cannot be discarded from GDOES measurements, but as will be discussed in the following sections, the hypothetical hydrogen incorporation cannot be electrically active. Lithium is not detected by the GDOES technique in any of the samples either. No (or very little) lithium incorporation is expected due to the lack of alkali diffusion barrier and the use of soda-lime glass substrates (SLG) substrates, letting the Li–Na exchange mechanism proposed by Yang et al.[67] take place, most likely suppressing Li and Na incorporation in the CZTSe matrix. However, Na signal is observed in the CZTSe layer due to the diffusion of sodium from the soda-lime glass, being most evident in the region between CZTSe and Mo, confirming the tendency of Na to segregate at the interfaces.[68] Another Na enrichment is present after 30 s of sputtering and is simultaneous with an increase of Zn and Se and the reduction of other elements (Sn, Cu). This behavior could be explained by the presence (at least in this
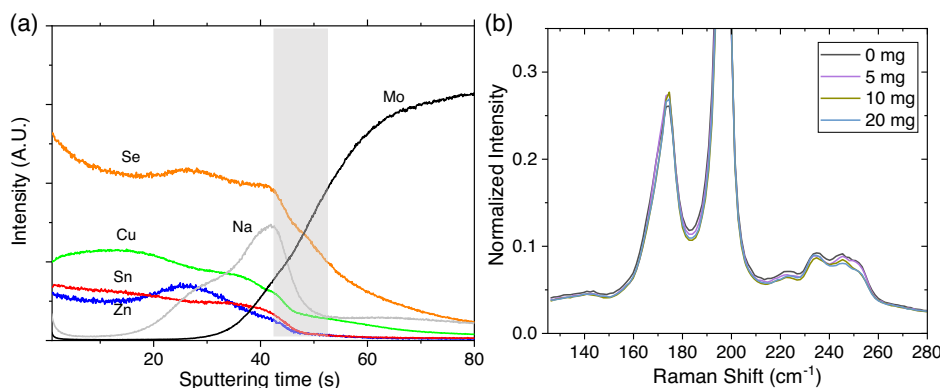
Figure 4. a) GDOES signal for Cu, Zn, Sn, Se, Na, and Mo in the 20 mg LiAlH$_4$ sample. Detection of Li, Al, and H was also tested resulting in no signal. b) Raman spectra of the one-step samples and only a reduction of 250 cm^{-1} is observed.

portion of the sample) of unreacted ZnSe with small grain size, where sodium is expected to segregate at the grain boundaries.

The values of E_g and E_u extracted from EQE measurements remain unchanged after the LiAlH$_4$ treatment and are shown in Figure 3b,c respectively.[69,70] An unchanged energy bandgap is consistent with no Li incorporation. However, similarly to hydrogen and H$_i$ defects, Li is expected to be present in the CZTSe matrix during reactive annealing, preventing Sn$_{Zn}$ by forming Li$_{Cu}$ defects, which slightly increases E_F during growth.[51] However, Li$_{Zn}$ formation energy has been predicted to decrease for higher E_F, probably having an impact on the maximum E_F during growth.[65,71] The Urbach Energy (E_u) is a parameter associated with sub-E_g absorption, generally related to band-tailing phenomena.[70] The effects of band tailing in CZTSe were first associated with Cu–Zn disorder; therefore, the effect of Cu–Zn disorder on the recombination rates has been thoroughly explored in the latter years and is still a matter of discussion, due to publications with contradictory results. Some reports claim it has no direct impact in the V_{oc} as improvements in electron mobility and lifetime have not always been detected for increasing order parameters.[28,32] Others argue it is a relevant parameter to be addressed for achieving high efficiencies.[30] A satisfactory insight into the role of Cu–Zn disorder based on ab initio calculations was proposed by Chen et al., where they showed that it contributed to increase the concentration of Sn$_{Zn}$ recombination centers.[72] The mechanism can be summarized as follows: Cu–Zn disorder tends to lower the Fermi Energy (E_F) of CZTSSe during growth. The lowered E_F in turn reduces the formation energy of donor-like defects, that is, Sn antisites. The increased presence of Sn$_{Zn}$ in disordered CZTSSe leads to increased Urbach tailing as a consequence of the enhanced presence of the [2Cu$_{Zn}$ + Sn$_{Zn}$] cluster, which was revealed to reduce E_g and was suggested to act as electron-trapping defects, eventually leading to Urbach-like band tailing. In addition, Gaussian E_g deviations emerge from partial kesterite to stannite transition (via [Cu$_{Zn}$ + Zn$_{Cu}$]$_\perp$[29] and no correlation has been shown with the presence of Sn-related deep defects.[29,72]

Furthermore, a Cu-rich/Zn-poor composition during growth is argued to have the same effects. In contrast, a Zn-rich composition results in increased E_F.[72] It is worth mentioning that Cu-rich conditions increase the single-phase CZTSe window,

justifying why the compositional change from Cu-rich to Cu-poor conditions has been successful.[73,74] However, Zn-rich compositions during growth are not easy to achieve due to the high stability of ZnSe.[23] In addition, reducing the Sn concentration in order to prevent Sn antisites is not a viable approach due to secondary phase formation (CuSe and Cu$_2$Se) which would have a strong detrimental effect in the device properties.[23] The fact that hole concentration is high under all compositional conditions (i.e., low E_F) due to high concentrations of Cu$_{Zn}$, due to both the poor Zn incorporation during growth and the low formation energy of the defect in all chemical conditions, has also been pointed out in ab initio publications.[13]

The Raman spectra shown in Figure 4b reveal a decreased area of the 250 cm^{-1} peak, associated with the commonly called B-type defect [2Zn$_{Cu}$ + Zn$_{Sn}$].[75] A reduced concentration of the B-type defect is probably associated with increased Sn$_{Sn}$ incorporation instead of Sn$_{Zn}$ (see Discussion). However, the reduced presence of Zn$_{Cu}$ defects, also suggested by the reasoning above, should imply a reduced area of the peak associated with the A-type defect [Zn$_{Cu}$ + V$_{Cu}$], which is not observed in the Raman spectra. The fact that the area of this peak remains unchanged can be explained by increased V$_{Cu}$ concentration. The areas related to the A-type and B-type defects are shown in more detail in Figure S5, Supporting Information.

In the framework of transient E_F upward shift and also in our samples, Li and H are expected to outgas from the absorber during cooling down after the high-temperature step. Sn disorder is not relevant at temperatures below the annealing temperaure.[72] Therefore, we assume Sn atoms remain practically fixed during the cooling-down step process, meaning that the deep-defect concentration also remains constant. Therefore, from the V_{oc} increase we infer a reduced Sn$_{Zn}$ defect density, this will be further discussed in the following sections. In addition, the doped samples show a reduced [2Zn$_{Cu}$ + Zn$_{Sn}$] and constant [Zn$_{Cu}$ + V$_{Cu}$] concentration as demonstrated by Raman spectroscopy. Finally, a constant E_u for all LiAlH$_4$-doped samples extracted from EQE is observed (and therefore constant concentration of [2Cu$_{Zn}$ + Sn$_{Zn}$]). The modification on the concentration of these defects necessarily implies a slight reduction of [Zn$_{Cu}$] and an increase of both [Cu$_{Zn}$] and [V$_{Cu}$], which should increase overall p-type doping. This is consistent with predictions

of a decreased concentration of donor defects (Zn_{Cu}) and an increased concentration of acceptor defects (Cu_{Zn} and V_{Cu}).[13] Naturally, the formation energy of neutral defect clusters is not strongly affected by slight modifications of E_F, consistent with DFT calculations,[72] [$2Zn_{Cu}+Zn_{Sn}$] an exception due to reaction kinetics not allowing Zn_{Sn} to be formed. This leads to the thinking that the shallow defect structure of CZTSe is slightly affected by the transient upward E_F shift. The effects are reduced as compared with Sn defects due to the decreased solubility of Li and H at the moment that Cu and Zn cations become practically fixed due to diffusion mitigation consequence of low temperature.

2.2. Electrical Characterization

Dark J-V curves shown in Figure S6, Supporting Information, were analyzed by performing a fitting using the single-diode model, allowing to extract the diode quality factor (n), series resistance (R_s), shunt resistance (R_{sh}), and reverse saturation current (J_0). The parameters for the best subcells of both the reference and the CZTSe-20mg sample are displayed in **Table 2**. It is straightforward that the improvement in the FF is directly related to the changes in both n and R_{sh}. The first parameter is slightly decreased while R_{sh} exhibits a fourfold increase. We attribute the increase in R_{sh} to the increase in grain growth, leading to an increased CZTSe/selective contact area and therefore less shunting paths. Nonradiative recombination at the SCR is limiting the V_{oc} in CZTSe solar cells, as mentioned in previous sections. The reduction of n indicates an increased recombination rate within the bulk compared with the SCR, where $p >> \Delta n$ implies lower nonradiative recombination rates.[76] Additionally, $LiAlH_4$ treatment implies a reduction by an order of magnitude of J_0. The latter strongly suggests decreased recombination rates.[77]

To support the electrical characterization results, photoluminescence quantum yield (PLQY) was measured on the devices. While nonradiative losses can be estimated directly from the PLQY by $kT \cdot ln(PLQY)$, the quasi-Fermi-level splitting (QFLS) can be estimated from fitting the high-energy slope of the absolute luminescence spectra.[78,79] Both PLQY and QFLS are shown in **Figure 5**a). It can be seen that the nonradiative losses significantly decrease with increasing hydride mass, while the QFLS increases accordingly and shows the same trend as the measured V_{oc}. The fact that the QFLS values increase with hydride doping and are 10-30 meV larger than the measured V_{oc} is further confirmation that the bulk electronic properties of the devices are improved. Although measurements on bare absorbers showed lower PLQY signals, we believe that this can be attributed to surface degradation and/or the importance of the heterojunction soft thermal treatment.

An increase in the QFLS may be caused by either a reduced recombination activity and thus a quasi-Fermi level for minority carriers closer to the (conduction) band or a higher doping level and thus a majority carrier quasi-Fermi level closer to the (valence) band. In order to extract the majority carrier concentration, capacitance–voltage profiles were measured at room temperature and 92 kHz. The extracted carrier concentrations are shown in Figure 5b for the different films. The carrier densities for all of the measured samples stay within the same order of magnitude; however, a monotonic increase in the carrier concentration (from $\approx 1.5 \times 10^{16}$ to $\approx 6.5 \times 10^{16}\,cm^{-3}$) estimated from the minimum of the capacitance–voltage (CV) profile is observed and is partially responsible for the QFLS improvement with $LiAlH_4$ doping. The hole concentration increase, as discussed earlier, is justified by a slight modification in the shallow defect concentration (Cu_{Zn}, Zn_{Cu}, and V_{Cu}). The incorporation of ionized donor H_i point defects would result in an opposite impact in hole concentration, suggesting that H is not incorporated in CZTSe bulk. Anyways, as mentioned previously, trace concentrations located at the grain boundaries or surface cannot be discarded. Nevertheless, a reduction of the

Table 2. Optoelectronic parameters of CZTSe best subcells. Parameters are obtained by illuminated J-V, dark J-V, EQE, PL, and C-V.

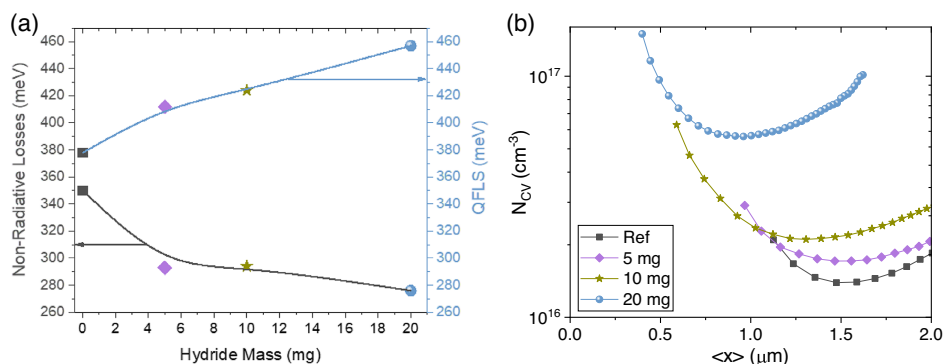| Sample	V_{oc} [mV]	J_{sc} [mA cm^{-2}]	FF [%]	PCE [%]	R_s [Ω cm^{-2}]	R_{sh} [Ω cm^{-2}]	n	J_0 [mA cm^{-2}]	E_g [eV]	E_u [meV]	W_{SCR} [nm]	τ_{e^-} [ps]
Ref	418	27.1	61.3	6.9	0.1	246	1.6	8×10^{-4}	1.03	22	200	60
20 mg	469	27.4	68.9	8.9	0.1	1028	1.4	6×10^{-5}	1.04	22	80	260

Figure 5. a) QFLS and nonradiative losses extracted from PL. Notice the decrease in nonradiative losses upon $LiAlH_4$ introduction while QFLS follows the V_{oc} of the devices. b) Carrier concentration as a function of the average distance from the junction extracted from C-V sweep at 92 kHz and 300 K.

SCR width implies a reduced region where the SRH mechanism shows higher recombination rates.

However, the change in the SCR width is not strong enough to increase the collection efficiency of electrons generated by long-wavelength photons; in fact, it should be detrimental for it; the possible origins for the increase in current and long-wavelength photon collection will be discussed in the following sections.

The minority carrier lifetime can be estimated from the PLQY and carrier density measurements as published previously.[80] Note that the real SRH lifetime is difficult to determine in CZTSSe due to the effect of carrier trapping/detrapping, which can lead to apparent lifetimes larger than 1 ns.[27] An increased lifetime is expected if the recombination center concentration is reduced. The estimated lifetimes of the reference and the 20 mg samples are shown in Table 1. We observe a remarkable increase on the minority carrier lifetime, from about 60 to 260 ps, resulting in a fourfold increase compared with the reference sample.

The increased minority carrier lifetime is consistent with both the reduced space–charge region recombination, indicated by a decreased diode ideality factor, and the increased V_{oc}. These observations are consistent with the hypothesis of reduced nonradiative recombination due to a lower Sn_{Zn} concentration.

3. Discussion

To shed light on the effects of the reduced [Sn_{Zn}] recombination center, 1D numerical analysis has been performed with SCAPS-1D software. In order to understand how the changes in the recombination center concentration and the majority carrier (hole) concentration affect the photovoltaic performance of the CZTSe material in the Mo/CZTSe/CdS/i-ZnO/ITO device configuration, both parameters are modified. Details regarding the baseline structure parameters considered are given in Table S2, Supporting Information.

To parametrize deep defect recombination, and thus the increase of lifetime, a bulk defect with the properties of Sn_{Zn} has been included, as shown in Table S3, Supporting Information. The concentration of the defect is adjusted to fit the lifetime obtained (60 and 260 ps respectively). This method overestimates the recombination rate, as the experimental measures are able to access the electron lifetime for minority carriers in the full-device configuration, and thus takes into account recombination losses at interfaces and window layer. Furthermore, the discrepancy between experimental and calculated J–V curves is limited as bulk (and specifically Sn_{Zn}) recombination dominates a large part of the recombination rates. However, the effects of the changes in lifetime and hole concentration parametrized in SCAPS-1D should be only discussed qualitatively. Hence, the shallow acceptor doping and the lifetime are simultaneously increased according to the measured values (Reference: $N_A = 1.5 \times 10^{16}\,cm^{-3}$ and $\tau_{e-} = 60\,ps$ and 20 mg $N_A = 6.5 \times 10^{16}$ and $\tau_{e-} = 260\,ps$) to verify if the improvements in the photovoltaic performance can be solely ascribed to these two parameters. As shown in **Figure 6**, it is clear that the improvement of V_{oc} is correlated with the increase of these two parameters. In addition, the increased FF correlates with
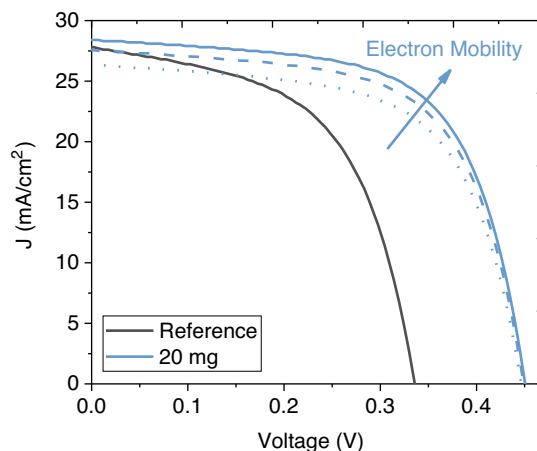

Figure 6. SCAPS-1D numerically calculated J-V curves. Black and blue color indicate the parametrized material properties implemented (Reference→ $N_A = 1.5 \times 10^{16}\,cm^{-3}$ and $\tau_{e-} = 60\,ps$ and 20 mg→ $N_A = 6.5 \times 10^{16}$ and $\tau_{e-} = 260\,ps$). According to the calculated curves, the increase in hole concentration should dominate the effect on the J_{sc} over the lifetime increase, and therefore current should decrease. As this is in disagreement with experimental observation, we propose increased electron mobility (with values $\mu_{e-} = 20$, 30 and 40 cm^2 V^{-1} s, for the dotted, dashed, and solid lines, respectively) to reproduce the increase in current, as discussed in the text.

the V_{oc} and is marginally affected when increasing R_{sh}. Surprisingly, the experimentally observed increase in J_{sc} is not reproduced by the calculated curves, that is, the increase in the lifetime does not compensate the reduction in current due to the increased hole density and reduced SCR width (Table 2). We hypothesize that a higher electron mobility (also shown in Figure 6) suffices to explain the increase in J_{sc}. While no experimental proof is provided here, the larger grain size could lead to reduced grain boundary scattering and therefore an improved mobility, an increase of the grain size correlated with an improvement of J_{sc}, has been experimentally observed by other groups.[59,60] In addition, the presence of alkali metals at the grain boundaries can lead to a hole reflector and electron attracter behavior, whose effect might be more noticeable in very low injection conditions, explaining the difference in the behavior in the EQE only for the LiAlH$_4$-treated samples.[33] This hypothesis leads to a possible additional benefit of the presence of small atoms during CZTSe formation and growth by passivating nonbenign grain boundaries, which in some CZTSe absorbers (with low carrier concentration) can dominate the recombination rates.

Finally, we propose a model of the interaction of small atoms (H and Li) during growth in the framework of defect chemistry. Therefore, we first describe the reaction process of undoped CZTSe. Due to the high stability of ZnSe, Zn incorporation is delayed as compared with Cu and Sn, as described in **Figure 7**. Therefore, the CZTSe film is Zn poor during the first stages of reactive annealing. In addition, Cu and Sn can be present in a 2+ oxidation state. Consequently, Zn vacancies are less stable in CZTSe as compared with cation antisites (i.e., Zn vacancies always show a higher formation energy than
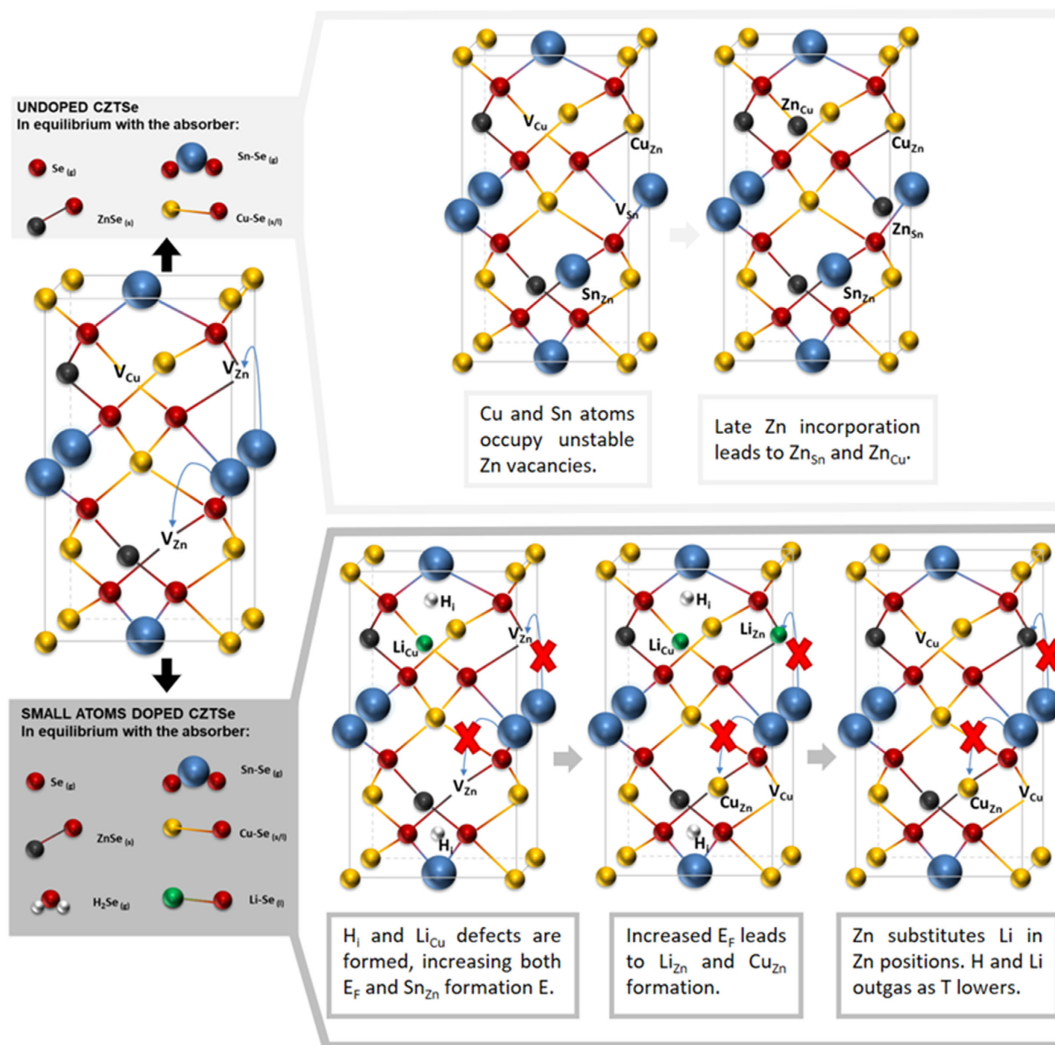
Figure 7. Schematics of CZTSe defect structure during reactive annealing. As mentioned in the body of the text, the starting point is a Zn-deficient CZTSe, due to the high ZnSe stability. This results in a V_{Zn}-rich structure, which is unstable upon the formation of Cu_{Zn} and Sn_{Zn}. The system's energy will be minimized if Zn vacancies are occupied. Top) Process for undoped CZTSe. Bottom) Process for small atom-doped CZTSe.

Cu_{Zn} and Sn_{Zn}), explaining the proliferation of Cu_{Zn} and Sn_{Zn} defects, as described in Figure 7 (top).[73] By the end of the high-temperature step, all Zn has been incorporated. However, Cu and Sn atoms remain at Zn positions, while Zn atoms occupy Cu and Sn sites.

In the case of small atom-doped CZTSe, a reduction in Sn_{Zn} concentration can be explained by the presence of Li_{Cu}, Li_{Zn}, and H_i. As described in Figure 7 (bottom), at the first stages of the reaction, when a small amount of $LiAlH_4$ is decomposed, the contribution of H_i to E_F upward shift can be expected. Therefore, Li would incorporate at Cu positions, forming Li_{Cu} and also increasing E_F if a Cu vacancy is occupied. Thus, during the first stages of the high-temperature step (CZTSe formation), the Fermi energy of small atom-doped CZTSe is expected to be upwardly shifted. As E_F keeps increasing, more Li will occupy Zn positions, forming acceptor Li_{Zn} (also Cu_{Zn} will be formed) and decreasing the already reduced (due to H_i) probability of Sn_{Zn}

formation. As both Cu and Zn positions are occupied by Li (Li_{Zn} and Cu_{Zn} presenting the lowered formation energy due to the shift of E_F and their acceptor behavior), more Sn is sterically bound at Sn positions (Sn_{Sn}), reducing the recombination center concentration. In this case, Zn is able to substitute Li atoms and incorporate at the CZTSe matrix at the Zn positions, reducing the density of Zn antisites. Finally, as the temperature lowers, H and Li solubility decrease and are forced to outgas the material or accumulate at the grain boundaries in very little quantities. The proposed defect reactions are presented and discussed in the Supporting Information.

4. Conclusion

In this work, the $LiAlH_4$ decomposition during the CZTSe selenization process has been thoroughly investigated. Only short

processes have improved the efficiency of the devices, suggesting that the overexposure to the hydride decomposition might be detrimental. As an incorporation of Li, Al, and H in the final film could not be detected, it is believed that these atoms provide CZTSe a transient treatment. On the one-step processes, an increased selenization rate and grain growth are observed, ascribed to the formation of alkali–Se fluxing phases. In this case, the efficiency of the devices is boosted by more than 2% in absolute and is mostly related to increases in both V_{oc} and FF. The electrical characterization shows a reduced diode ideality factor and J_0 while the series resistance remains constant, indicating a reduction in nonradiative recombination further supported by a minority carrier lifetime increase by an order of magnitude. C-V profiling reveals an increased carrier concentration. The complementary drift-diffusion numerical analysis shows that an increased carrier concentration and decreased bulk recombination lead to increased V_{oc} and decreased J_{sc}, which indicate a likely additional increase in the electron mobility to explain the observed increased J_{sc}. A detailed model of the CZTSe formation and growth from a defect chemistry approach is presented to explain the reduction of CZTSe recombination center concentration (Sn_{Zn}) and the increase in carrier concentration (V_{Cu}, Cu_{Zn}, and Zn_{Cu}), consistent with unchanged E_g and E_u values and consistent with the Raman analysis.

In summary, the use of $LiAlH_4$ during reactive annealing reveals a simple and promising pathway to further improve the CZTSe efficiency due to its ability to address several of the main CZTSe limiting factors at once, bulk recombination being the most relevant one. A clear beneficial impact on the selenization rate, grain growth (and therefore contact homogeneity), majority carrier concentration, and front contact has been demonstrated. Further optimization and understanding of the process might enable greatly improved performance of the CZTSe-based solar cell devices. The effects of small atom transient doping seem to indicate that an upwardly shifted E_F during growth is an effective method to improve the CZTSe bulk properties for photovoltaic applications owing to its ability to modify the defect structure without affecting the secondary phase formation.

5. Experimental Section

Sample Preparation: Samples were prepared on Mo-coated (DC magnetron sputtering, Alliance AC450) SLG substrates. A standard Cu/Sn/Cu/Zn metallic precursor stack was sequentially deposited on top of a Mo trilayer by DC sputtering. Back contact optimization and structure is explained in the study by Lopez-Marino et al.[81] The precursor composition and thickness was calibrated and measured by X-ray fluorescence (XRF, Fischerscope XDV), precursors with Cu/(Sn + Zn) = 0.70 and Zn/Sn = 1.05 ratios were used. The as-deposited stack was subjected to reactive annealing under Se + Sn atmosphere (100 mg of Se (Alfa-Aesar powder, 200 mesh, 99.999%) and 5 mg of Sn (Alfa-Aesar powder, 100 mesh, 99.995%)) and different masses of $LiAlH_4$ (Sigma-Aldrich powder, reagent, 95.0%) (0, 5, 10, and 20 mg). The process was repeated for different thermal profiles using graphite boxes (69 cm³ in volume) in a conventional tubular furnace, as shown in Figure S1a, Supporting Information and described. 1) One step: dwelling time of 15 min with a ramp of 20 °C min⁻¹ and temperature of 550 °C under Ar static pressure (950 mbar) and 2) two steps: first step with a dwelling time of 30 min with a ramp of 20 °C min⁻¹ and temperature of 400 °C at 1.5 mbar (Ar flux) and second step with dwelling

time of 15 min with a ramp of 20 °C min⁻¹ and temperature of 550 °C under Ar static pressure (1 bar)

Solar cell devices were fabricated by depositing 50 nm CdS by chemical bath deposition (CBD) preceded by several chemical etchings in order to remove secondary phases on the surface of the absorber and to passivate it, followed by deposition of 50 nm i-ZnO and 200 nm ITO by DC-pulsed sputtering (Alliance CT100).[24,25,82] To perform the optoelectronic characterization, 3×3 mm² subcells were mechanically scribed using a manual microdiamond scriber (OEG Optical Metrology MR200). Neither ARC nor metallic grids were used for the optoelectronic characterization of the devices. Air hotplate annealing was performed on the full devices for 25 min at 250 °C, including the heating ramp from room temperature.

Device and Material Characterization: Dark and illuminated J-V curves were measured using a calibrated Sun 3000 class AAA solar simulator (Abet Technologies, 25 °C, AM1.5G illumination) under ambient conditions. The spectral response was measured using a Bentham PVE300 system calibrated with Si and Ge photodiodes in order to obtain the external quantum efficiency (EQE) of the solar cells. Reflectance was measured using a built-in integrating sphere accessory in the spectral response equipment. Scanning electron microscopy (SEM) images were recorded on a ZEISS Series Auriga microscope utilizing an electron beam with 5 kV accelerating voltage. Room-temperature capacitance–voltage measurements (C–V) were carried out using an impedance analyzer from Novocontrol Technologies. A parallel circuit model was assumed to derive the device capacitance. From C–V measurements, doping profiles were calculated using the formalism of Miller and a relative dielectric permittivity of $\varepsilon = 8.5$ for CZTSe.[83]

Glow Discharge Optical Emission Spectroscopy (GDOES): A depth profiling analysis of composition on some selected samples was performed by GDOES measurements using a Horiba Jobin Yvon GD Profiler 2 spectrometer, equipped with an anode diameter of 4 mm and 19 element channels.

Photoluminescence (PL): Absolute photon number-calibrated CZTSe PL spectra were obtained with 660 nm excitation under AM1.5-equivalent illumination intensity. Hyperspectral luminescence images were obtained using a Peltier-cooled InGaAs camera together with a liquid crystal tunable bandpass filter. The system was calibrated for absolute photon counts using an integrating sphere and a calibrated halogen light source.

Raman spectroscopy: Raman spectra were obtained using a micro-Raman (Renishaw's inVia Qontor) microscope. Excitation wavelength was 532 nm with a nominal incident power of 1 mW and a spot size of 0.25 µm. Nine spectra were obtained at different surface points for each sample, normalized averages are presented in the body of the text. The position of all spectra was corrected by taking into account the first-order Raman spectrum of monocrystalline silicon as a reference measured before each acquisition and imposing its position at 520 cm⁻¹.

Supporting Information

Supporting Information is available from the Wiley Online Library or from the author.

Acknowledgements

Conflict of Interest

The authors declare no conflict of interest.

Data Availability Statement

The data that support the findings of this study are available from the corresponding author upon reasonable request.

Keywords

[1] M. Green, K. Emery, Y. Hishikawa, W. Warta, E. D. Dunlop, *IEEE Trans. Fuzzy Syst.* **2012**, *20*, 1114.

[2] M. Nakamura, K. Yamaguchi, Y. Kimoto, Y. Yasaki, T. Kato, H. Sugimoto, *IEEE* **2019**, *9*, 1863.

[3] A. F. Solar, *First Solar, Inc.; First Solar Achieves Yet Another Cell Conversion Efficiency World Record*, https://investor.firstsolar.com/news/press-release-details/2016/First-Solar-Achieves-Yet-Another-Cell-Conversion-Efficiency-World-Record/default.aspx. (accessed: September 2022).

[4] S. Delbos, *EPJ Photovoltaics* **2012**, *3*, 35004.

[5] X. Liu, Y. Feng, H. Cui, F. Liu, X. Hao, G. Conibeer, D. B. Mitzi, M. Green, *Prog. Photovoltaics Res. Appl.* **2016**, *24*, 879.

[6] S. Giraldo, Z. Jehl, M. Placidi, V. Izquierdo-Roca, A. Pérez-Rodríguez, E. Saucedo, *Adv. Mater.* **2019**, *31*, 1806692.

[7] W. Wang, M. T. Winkler, O. Gunawan, T. Gokmen, T. K. Todorov, Y. Zhu, D. B. Mitzi, *Adv. Energy Mater.* **2014**, *4*, 1301465.

[8] D.-H. Son, S.-H. Kim, S.-Y. Kim, Y.-I. Kim, J.-H. Sim, S.-N. Park, D.-H. Jeon, D.-K. Hwang, S.-J. Sung, J.-K. Kang, K.-J. Yang, D.-H. Kim, *J. Mater. Chem. A* **2019**, *7*, 25279.

[9] J. Li, Y. Huang, J. Huang, G. Liang, Y. Zhang, G. Rey, F. Guo, Z. Su, H. Zhu, L. Cai, K. Sun, Y. Sun, F. Liu, S. Chen, X. Hao, Y. Mai, M. A. Green, *Adv. Mater.* **2020**, *32*, 2005268.

[10] C. Yan, J. Huang, K. Sun, S. Johnston, Y. Zhang, H. Sun, A. Pu, M. He, F. Liu, K. Eder, L. Yang, J. M. Cairney, N. J. Ekins-Daukes, Z. Hameiri, J. A. Stride, S. Chen, M. A. Green, X. Hao, *Nat. Energy* **2018**, *3*, 764.

[11] J. Zhou, X. Xu, H. Duan, H. Wu, J. Shi, Y. Luo, D. Li, Q. Meng, *Nano Energy* **2021**, *89*, 106405.

[12] R. Fonoll-Rubio, J. Andrade-Arvizu, J. Blanco-Portals, I. Becerril-Romero, M. Guc, E. Saucedo, F. Peiró, L. Calvo-Barrio, M. Ritzer, C. S. Schnohr, S. Estradé, V. Izquierdo-Roca, A. Pérez-Rodríguez, *Energy Environ. Sci.* **2021**, *14*, 507.

[13] S. Kim, J. A. Márquez, T. Unold, A. Walsh, *Energy Environ. Sci.* **2020**, *13*, 1481.

[14] K. F. Tai, O. Gunawan, M. Kuwahara, S. Chen, S. G. Mhaisalkar, C. H. A. Huan, D. B. Mitzi, *Adv. Energy Mater.* **2016**, *6*, 1501609.

[15] J. Li, M. Wei, Q. Du, W. Liu, G. Jiang, C. Zhu, *Surf. Interface Anal.* **2013**, *45*, 682.

[16] Y. Sun, H. Guo, P. Qiu, S. Zhang, S. Wang, L. Wu, J. Ao, Y. Zhang, *J. Energy Chem.* **2021**, *57*, 618.

[17] M. He, K. Sun, M. P. Suryawanshi, J. Li, X. Hao, *J. Energy Chem.* **2021**, *60*, 1.

[18] L. Yin, G. Cheng, Y. Feng, Z. Li, C. Yang, X. Xiao, *RSC Adv.* **2015**, *5*, 40369.

[19] M. Courel, J. A. Andrade-Arvizu, O. Vigil-Galán, *Mater. Res. Express* **2016**, *3*, 095501.

[20] F. Martinho, S. Lopez-Marino, M. Espíndola-Rodríguez, A. Hajijafarassar, F. Stulen, S. Grini, M. Döbeli, M. Gansukh, S. Engberg, E. Stamate, L. Vines, J. Schou, O. Hansen, S. Canulescu, *ACS Appl. Mater. Interfaces* **2020**, *12*, 39405.

[21] A. Zhang, Z. Song, Z. Zhou, Y. Deng, W. Zhou, S. Yuan, D. Kou, X. Zhang, Y. Qi, S. Wu, *ACS Appl. Energy Mater.* **2020**, *3*, 10976.

[22] M. S. Lyam, T. Hölscher, M. Maiberg, A. Cabas-Vidani, A. Hernandez-Martinez, H. Tampo, R. Scheer, *J. Appl. Phys.* **2021**, *129*, 205703.

[23] G. Altamura, J. Vidal, *Chem. Mater.* **2016**, *28*, 3540.

[24] S. López-Marino, Y. Sánchez, M. Placidi, A. Fairbrother, M. Espindola-Rodríguez, X. Fontané, V. Izquierdo-Roca, J. López-García, L. Calvo-Barrio, A. Pérez-Rodríguez, E. Saucedo, *Chem. - A Eur. J.* **2013**, *19*, 14814.

[25] H. Xie, Y. Sánchez, S. López-Marino, M. Espíndola-Rodríguez, M. Neuschitzer, D. Sylla, A. Fairbrother, V. Izquierdo-Roca, A. Pérez-Rodríguez, E. Saucedo, *ACS Appl. Mater. Interfaces* **2014**, *6*, 12744.

[26] S. Schorr, G. Gurieva, M. Guc, M. Dimitrievska, A. Pérez-Rodríguez, V. Izquierdo-Roca, C. S. Schnohr, J. Kim, W. Jo, J. M. Merino, *J. Phys Energy* **2020**, *2*, 012002.

[27] C. J. Hages, A. Redinger, S. Levcenko, H. Hempel, M. J. Koeper, R. Agrawal, D. Greiner, C. A. Kaufmann, T. Unold, *Adv. Energy Mater.* **2017**, *7*, 1700167.

[28] S. Bourdais, C. Choné, B. Delatouche, A. Jacob, G. Larramona, C. Moisan, A. Lafond, F. Donatini, G. Rey, S. Siebentritt, A. Walsh, G. Dennler, *Adv. Energy Mater.* **2016**, *6*, 1502276.

[29] A. Crovetto, S. Kim, M. Fischer, N. Stenger, A. Walsh, I. Chorkendorff, P. C. K. Vesborg, *Energy Environ. Sci.* **2020**, *13*, 3489.

[30] T. Gokmen, O. Gunawan, T. K. Todorov, D. B. Mitzi, *Appl. Phys. Lett.* **2013**, *103*, 103506.

[31] M. H. Wolter, R. Carron, E. Avancini, B. Bissig, T. P. Weiss, S. Nishiwaki, T. Feurer, S. Buecheler, P. Jackson, W. Witte, S. Siebentritt, *Prog. Photovoltaics Res. Appl.* **2022**, *30*, 702.

[32] H. Hempel, R. Eichberger, I. Repins, T. Unold, *Thin Solid Films* **2018**, *666*, 40.

[33] W.-J. Yin, Y. Wu, S.-H. Wei, R. Noufi, M. M. Al-Jassim, Y. Yan, *Adv. Energy Mater.* **2014**, *4*, 1300712.

[34] J. Kim, G. Y. Kim, T. T. T. Nguyen, S. Yoon, Y.-K. Kim, S.-Y. Lee, M. Kim, D.-H. Cho, Y.-D. Chung, J.-H. Lee, M.-J. Seong, W. Jo, *Phys. Chem. Chem. Phys.* **2020**, *22*, 7597.

[35] H. Xin, S. M. Vorpahl, A. D. Collord, I. L. Braly, A. R. Uhl, B. W. Krueger, D. S. Ginger, H. W. Hillhouse, *Phys. Chem. Chem. Phys.* **2015**, *17*, 23859.

[36] S. Kim, J.-S. Park, S. N. Hood, A. Walsh, *J. Mater. Chem. A* **2019**, *7*, 2686.

[37] S. Kim, J.-S. Park, A. Walsh, *ACS Energy Lett.* **2018**, *3*, 496.

[38] T. C. Harman, P. J. Taylor, D. L. Spears, M. P. Walsh, *Int. Conf. Thermoelectr. ICT, Proc.* **1999**, *999*, 280.

[39] S. N. Hood, A. Walsh, C. Persson, K. Iordanidou, D. Huang, M. Kumar, Z. Jehl, M. Courel, J. Lauwaert, S. Lee, *J. Phys Energy* **2019**, *1*, 042004.

[40] S. Kim, S. N. Hood, A. Walsh, *Phys. Rev. B* **2019**, *100*, 5.

[41] B. Das, I. Aguilera, U. Rau, T. Kirchartz, *Phys. Rev. Mater.* **2020**, *4*, 1.

[42] J. Li, Z.-K. Yuan, S. Chen, X.-G. Gong, S.-H. Wei, *Chem. Mater.* **2019**, *31*, 826.

[43] S. Li, M. A. Lloyd, H. Hempel, C. J. Hages, J. A. Márquez, T. Unold, R. Eichberger, B. E. Mccandless, J. B. Baxter, *Phys. Rev. Appl.* **2019**, *11*, 1.

[44] Z.-K. Yuan, S. Chen, Y. Xie, J.-S. Park, H. Xiang, X.-G. Gong, S.-H. Wei, *Adv. Energy Mater.* **2016**, *6*, 1601191.

[45] Y. Du, S. Wang, Q. Tian, Y. Zhao, X. Chang, H. Xiao, Y. Deng, S. Chen, S. Wu, S. (Frank) Liu, *Adv. Funct. Mater.* **2021**, *31*, 2010325.

[46] S. Giraldo, C. M. Ruiz, M. Espíndola-Rodríguez, Y. Sánchez, M. Placidi, D. Cozza, D. Barakel, L. Escoubas, A. Pérez-Rodríguez, E. Saucedo, *Sol. Energy Mater. Sol. Cells* **2016**, *151*, 44.

[47] D.-H. Kuo, M. Tsega, *Jpn. J. Appl. Phys.* **2014**, *53*, 035801.

[48] J. B. Varley, V. Lordi, T. Ogitsu, A. Deangelis, K. Horsley, N. Gaillard, *J. Appl. Phys.* **2018**, *123*, 161408.

[49] K. Otte, G. Lippold, H. Neumann, A. Schindler, *J. Phys. Chem. Solids* **2003**, *64*, 1641.

[50] S. Grini, H. Aboulfadl, N. Ross, C. Persson, C. Platzer-Björkman, M. Thuvander, L. Vines, *Phys. Status Solidi Basic Res.* **2020**, *257*, 2000062.

[51] T. Maeda, A. Kawabata, T. Wada, *Phys. Status Solidi Curr. Top. Solid State Phys.* **2015**, *12*, 631.

[52] T. Todorov, H. W. Hillhouse, S. Aazou, Z. Sekkat, O. Vigil-Galán, S. D. Deshmukh, R. Agrawal, S. Bourdais, M. Valdés, P. Arnou, D. B. Mitzi, P. J. Dale, *J. Phys. Energy* **2020**, *2*, 012003.

[53] J. Park, J. Huang, J. Yun, F. Liu, Z. Ouyang, H. Sun, C. Yan, K. Sun, K. Kim, J. Seidel, S. Chen, M. A. Green, X. Hao, *Adv. Energy Mater.* **2018**, *8*, 1701940.

[54] R. A. Varin, L. Zbroniec, *J. Alloys Compd.* **2010**, *504*, 89.

[55] Z. Shen, S. Wang, Y. Liu, Y. Sun, J. Wu, H. Guo, K. Zhang, S. Zhang, F. Liu, Y. Zhang, *J. Energy Chem.* **2021**, *62*, 637.

[56] S. G. Haass, C. Andres, R. Figi, C. Schreiner, M. Bürki, Y. E. Romanyuk, A. N. Tiwari, *Adv. Energy Mater.* **2018**, *8*, 1701760.

[57] D. Wang, J. Chen, M. Wu, S. Gao, L. Wu, J. Ao, Y. Sun, Y. Zhang, *Sol. Energy Mater. Sol. Cells* **2019**, *198*, 35.

[58] A. Cabas-Vidani, S. G. Haass, C. Andres, R. Caballero, R. Figi, C. Schreiner, J. A. Márquez, C. Hages, T. Unold, D. Bleiner, A. N. Tiwari, Y. E. Romanyuk, *Adv. Energy Mater.* **2018**, *8*, 1801191.

[59] B. Xu, X. Qin, X. Lu, Y. Liu, Y. Chen, H. Peng, P. Yang, J. Chu, L. Sun, *Sol. RRL* **2021**, *5*, 2100216.

[60] J. Li, J. Huang, J. Cong, Y. Mai, Z. Su, G. Liang, A. Wang, M. He, X. Yuan, H. Sun, C. Yan, K. Sun, N. J. Ekins-Daukes, M. A. Green, X. Hao, *Small* **2022**, *18*, 2105044.

[61] Y. Gong, Y. Zhang, Q. Zhu, Y. Zhou, R. Qiu, C. Niu, W. Yan, W. Huang, H. Xin, *Energy Environ. Sci.* **2021**, *14*, 2369.

[62] Y. Sun, P. Qiu, W. Yu, J. Li, H. Guo, L. Wu, H. Luo, R. Meng, Y. Zhang, S. (Frank) Liu, *Adv. Mater.* **2021**, *33*, 2104330.

[63] Y. Gong, R. Qiu, C. Niu, J. Fu, E. Jedlicka, R. Giridharagopal, Q. Zhu, Y. Zhou, W. Yan, S. Yu, J. Jiang, S. Wu, D. S. Ginger, W. Huang, H. Xin, *Adv. Funct. Mater.* **2021**, *31*, 2101927.

[64] X. Xu, L. Guo, J. Zhou, B. Duan, D. Li, J. Shi, H. Wu, Y. Luo, Q. Meng, *Adv. Energy Mater.* **2021**, *11*, 2102298.

[65] K. Zhao, H. Xiang, Y. Cui, R. Zhu, C. Liu, Y. Jia, *Appl. Phys. Lett.* **2021**, *118*, 252106.

[66] G. A. Steigmann, J. Goodyear, *Acta Crystallogr.* **1966**, *20*, 617.

[67] Y. Yang, L. Huang, D. Pan, *ACS Appl. Mater. Interfaces* **2017**, *9*, 23878.

[68] H. Xie, S. López-Marino, T. Olar, Y. Sánchez, M. Neuschitzer, F. Oliva, S. Giraldo, V. Izquierdo-Roca, I. Lauermann, A. Pérez-Rodríguez, E. Saucedo, *ACS Appl. Mater. Interfaces* **2016**, *8*, 5017.

[69] R. Carron, C. Andres, E. Avancini, T. Feurer, S. Nishiwaki, S. Pisoni, F. Fu, M. Lingg, Y. E. Romanyuk, S. Buecheler, A. N. Tiwari, *Thin Solid Films* **2019**, *669*, 482.

[70] J. Chantana, Y. Kawano, T. Nishimura, A. Mavlonov, T. Minemoto, *Sol. Energy Mater. Sol. Cells* **2020**, *210*, 110502.

[71] M. He, X. Zhang, J. Huang, J. Li, C. Yan, J. Kim, Y.-S. Chen, L. Yang, J. M. Cairney, Y. Zhang, S. Chen, J. Kim, M. A. Green, X. Hao, *Adv. Energy Mater.* **2021**, *11*, 2003783.

[72] W. Chen, D. Dahliah, G.-M. Rignanese, G. Hautier, *Energy Environ. Sci.* **2021**, *14*, 3567.

[73] T. Ratz, N. D. Nguyen, G. Brammertz, B. Vermang, J.-Y. Raty, *J. Mater. Chem. A* **2022**, *10*, 4355.

[74] D. Pareek, T. Taskesen, J. A. Márquez, H. Stange, S. Levcenco, I. Simsek, D. Nowak, T. Pfeiffelmann, W. Chen, C. Stroth, M. H. Sayed, U. Mikolajczak, J. Parisi, T. Unold, R. Mainz, L. Gütay, *Sol. RRL* **2020**, *4*, 2000124.

[75] M. Dimitrievska, F. Oliva, M. Guc, S. Giraldo, E. Saucedo, A. Pérez-Rodríguez, V. Izquierdo-Roca, *J. Mater. Chem. A* **2019**, *7*, 13293.

[76] J. Hüpkes, U. Rau, T. Kirchartz, *Sol. RRL* **2022**, *6*, 2100720.

[77] A. Cuevas, *Energy Procedia* **2014**, *55*, 53.

[78] R. T. Ross, *J. Chem. Phys.* **1967**, *46*, 4590.

[79] D. Abou-Ras, T. Kirchartz, U. Rau, *Advanced Characterization Techniques For Thin Film Solar Cells: Second Edition*, Vol. 1–2, Wiley, USA **2016**.

[80] A. Redinger, S. Levcenko, C. J. Hages, D. Greiner, C. A. Kaufmann, T. Unold, *Appl. Phys. Lett.* **2017**, *110*, 122104.

[81] S. Lopez-Marino, M. Espíndola-Rodríguez, Y. Sánchez, X. Alcobé, F. Oliva, H. Xie, M. Neuschitzer, S. Giraldo, M. Placidi, R. Caballero, V. Izquierdo-Roca, A. Pérez-Rodríguez, E. Saucedo, *Nano Energy* **2016**, *26*, 708.

[82] M. Neuschitzer, Y. Sanchez, S. López-Marino, H. Xie, A. Fairbrother, M. Placidi, S. Haass, V. Izquierdo-Roca, A. Perez-Rodriguez, E. Saucedo, *Prog. Photovoltaics Res. Appl.* **2015**, *23*, 1660.

[83] G. L. Miller, *IEEE Trans. Electron Devices* **1972**, *19*, 1103.